ChemComm

COMMUNICATION

View Article Online
View Journal | View Issue

Cite this: *Chem. Commun.*, 2019, 55, 2078

Received 3rd January 2019,
Accepted 21st January 2019

DOI: 10.1039/c9cc00051h

rsc.li/chemcomm

Template synthesis of defect-rich MoS_2-based assemblies as electrocatalytic platforms for hydrogen evolution reaction†

Antonia Kagkoura,[a] Iordanis Tzanidis,[b] Vassilios Dracopoulos,[c] Nikos Tagmatarchis *[a] and Dimitrios Tasis*[bc]

Defect-rich MoS_2 nanostructures were synthesized in solution by a microwave-assisted process, employing either a sacrificial soft template ($CaCO_3$) or a non-sacrificial hard template (graphene oxide) and the electrocatalytic performance towards the hydrogen evolution reaction was found to be superior for the latter.

Transition metal dichalcogenides (TMDs) possess a stacked arrangement, in which atomic metal sheets are sandwiched by chalcogen ones, forming a 2D layered framework. When the multiple weak van der Waals interactions keeping together those layers are overcome, chemical exfoliation from the bulk occurs yielding few-layered TMDs. In fact, depending on the agents employed for the exfoliation process, diverse polytypes of TMDs are obtained, possessing metallic or semiconducting properties.[1–4] Considering merits attributed to electrocatalytic properties and stability, TMDs recently received high interest for the hydrogen evolution reaction (HER).[5–16] This is mainly due to specific characteristics of TMDs, the high electrical conductivity along the TMD layer and the tunable electronic properties.[17] Furthermore, the HER activity for TMDs stems from defect sites, mainly located in the periphery, contrasting the catalytically inert basal planes.[18] Interestingly, the population of defect sites may be adjusted by the adopted synthetic bottom-up approach of TMDs and/or the presence of an additional component, playing the role of electrocatalyst substrate. The introduction of defects at MoS_2 enhances electrocatalytic activity by cracking the crystal and consequently increasing the accessible internal surface area.[19,20] Therefore, in order to enhance the electrocatalytic properties of TMDs, it is important to develop novel TMD-based nanostructures with higher number of exposed catalytic sites.[21]

Of all the general protocols for preparing TMD-based nanostructures with a structural motif bearing an increased density of active sites, the most popular ones concern low temperature and short-time processes, such as solvothermal reduction reactions of a precursor salt. Specifically, microwave-assisted reduction of ammonium tetrathiomolybdate (ATTM) in DMF yielded MoS_2-based nanostructures with variable stacking order at 190–260 °C.[8,22] In parallel, the promotion of heterogeneous nucleation/growth of MoS_2 in liquid phase occurs in the presence of a hard template, such as oxidized carbon nanotubes[23] or graphene oxide sheets.[22,24,25] However, it is not known and surely deserves investigation the utilization of sacrificial templates en route the preparation of MoS_2-based nanostructures, under microwave conditions. In addition, although the structural and electrocatalytic properties of the aforementioned MoS_2-based hybrids with graphitic components were adequately addressed, a detailed study on the effect of component composition to the HER electrocatalytic activity has yet to be performed and assessed.

Considering the aforementioned points, the aim of the current work was the template synthesis of defect-rich MoS_2 nanosheets, with high specific surface area and subsequently their evaluation as HER electrocatalysts. Specifically, to realize this aim, we report the microwave-assisted bottom-up synthesis of MoS_2 in the presence of $CaCO_3$ as template, which can be selectively removed by acidic treatment. In parallel, the preparation of MoS_2-based nanostructures by employing graphene oxide (GO) as hard template was accomplished. The effect of the starting composition of the agents utilized, on the morphology and electrocatalytic activity of the MoS_2-based materials, was screened by examining different mass ratios between the inorganic precursor ATTM (employed in different concentrations 1–10 mg mL^{-1}) and the template (for details see ESI†).

The synthetic protocol for preparing defect-rich MoS_2 was based on the microwave-assisted reduction of ATTM in

[a] *Theoretical and Physical Chemistry Institute, National Hellenic Research Foundation, 48 Vassileos Constantinou Avenue, 11635 Athens, Greece. E-mail: tagmatar@eie.gr*
[b] *Department of Chemistry, University of Ioannina, 45110 Ioannina, Greece. E-mail: dtassis@cc.uoi.gr*
[c] *Foundation of Research and Technology, Hellas – Institute of Chemical Engineering Sciences, FORTH/ICEHT, Stadiou Str., Platani Rion, P.O. Box 1414, 26504 Patras, Greece*

† Electronic supplementary information (ESI) available: Experimental procedures and additional spectroscopic, thermal and microscopy imaging data. See DOI: 10.1039/c9cc00051h

solvothermal conditions at 230 °C. The wetting medium, DMF, played the role of reducing agent as its absence did not allow the formation of MoS_2. The sacrificial template $CaCO_3$, which was added in relative excess (two- to four-fold compared to ATTM), allowing the growth of MoS_2 within the confined space between $CaCO_3$ crystallites, was removed by acidic treatment to obtain MoS_2 nanostructures with variable morphology. Conversely, when using GO as "hard" template, MoS_2/reduced graphene oxide (rGO) nanostructures were obtained, due to thermal deoxygenation of the graphitic lattice.[26] Different $ATTM_x/GO_y$ amounts and mass ratios were treated under microwave irradiation, where x and y denote the corresponding mass of each component employed. Six different materials **1–6** were synthesized, by reacting $ATTM_{20}/GO_{12}$, $ATTM_{10}/GO_6$, $ATTM_5/GO_3$, $ATTM_5/GO_6$, $ATTM_{25}/GO_6$, and $ATTM_{50}/GO_6$, respectively (see ESI†).

X-ray diffraction from MoS_2-based nanostructures (Fig. 1a), gave a clear picture about the amorphous character of the stacked nanosheets. This is in full agreement with a recent work,[8] which demonstrated that MoS_2 crystallinity was enhanced at even higher temperatures than those currently employed. In addition, no stacking order was observed for rGO. Notably, the UV-Vis electronic absorption spectra of MoS_2/rGO hybrids lack the characteristic excitonic bands attributed to the semiconducting polytype. Instead, a broad absorption band in the visible region occupies the spectra (Fig. S1, ESI†), showcasing the metallic character of MoS_2 in all **1–6** hybrids.

The thermal stability of MoS_2 derived by the sacrificial template approach (sa-MoS_2), was examined by thermogravimetric analysis (TGA) under N_2. In Fig. S2 (ESI†), TGA profiles of the different sa-MoS_2 synthesized are presented and compared. It was observed that three sa-MoS_2 samples, prepared by the same starting concentration of ATTM with the one employed for untemplated MoS_2, were found to decompose appreciably up to 800 °C, with a total mass loss in the range 22–29%. In sharp contrast, untemplated MoS_2 showed a corresponding mass loss of about 60% (Fig. 1b). Such thermal profiles implied the existence of defect sites at the MoS_2 lattice, since parent bulk MoS_2 powder shows enhanced thermal stability.[27] Furthermore, the thermal stability of MoS_2/rGO hybrids **1–6** as obtained by the "hard template" approach, was assessed by TGA. In Fig. 1b, the TGA profiles of reference samples, MoS_2 synthesized in the absence of a template under microwave conditions and neat GO powder, as well as MoS_2/rGO **1** are presented and compared. The TGA graphs for materials **2–6** are shown at ESI† (Fig. S3). For GO, a 30% mass loss was observed at 150–350 °C, where the majority of the oxygen-related functionalities are thermally detached by the graphitic surface.[28] Further mass loss was mainly attributed to thermal decomposition of defected carbon network. As expected, MoS_2/rGO hybrids exhibited lower mass loss, when compared to the reference sample of GO, due to the absence of oxygen-containing labile groups. Assuming that at 200–800 °C the vast majority of the observed mass loss in the hybrids is attributed to the defected MoS_2-based nanostructures, a rough calculation of MoS_2 wt% content can be done for each hybrid. For example, **1** was found to contain about 40 wt% MoS_2. On the contrary, material **5** seems to contain almost double amount, approximately 75 wt%, of the inorganic component.

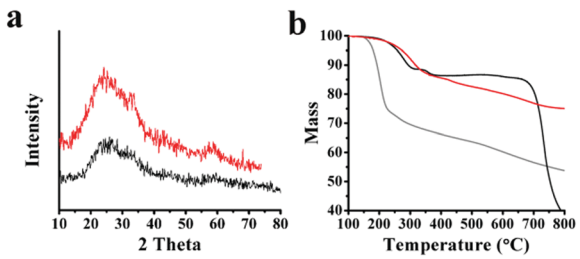

Fig. 1 (a) X-ray diffraction profiles for MoS_2/rGO material **1** (red) and sa-MoS_2 (black). (b) TGA graphs for MoS_2/rGO material **1** (red), untemplated MoS_2 (black) and GO (grey), obtained under N_2 flow.

To confirm the deoxygenation of graphitic lattice leading to reduction of graphene oxide to rGO, we performed vibrational spectroscopy measurements. In the IR spectrum of GO, typical bands corresponding to various stretching modes of C–O (at 1036 and 1220 cm^{-1}), C=C (at 1627 cm^{-1}) and C=O bonding (at 1715 cm^{-1}) were evident (Fig. S4, ESI†). After the microwave-assisted process, it was clear that in material **1** the bands corresponding to the carbon–oxygen bonding were disappeared, implying an efficient deoxygenation of the graphitic surface. The efficient reduction of the GO template during the microwave-assisted growth of MoS_2 nanostructures was further supported by Raman spectroscopy.

Raman spectra (λ_{exc} 633 nm) of sa-MoS_2 revealed characteristic modes due to MoS_2 (Fig. S5, ESI†), regardless of the starting composition of the components. In more detail, bands of MoS_2 at 373, 404 and 452 cm^{-1} were recorded, corresponding to in-plane E^1_{2g}, out-of-plane A_{1g} and 2LA(M) mode, respectively. The latter one was associated with disorder and defects. In addition, bands of MoS_2 at lower frequencies assigned to the A_{1g}(M)–LA(M) mode at 184 cm^{-1} and J_1, J_2 and J_3 modes at 150, 224 and 325 cm^{-1}, respectively, were identified. Notably, the J_1–J_3 phonon modes unveil the metallic polytype 1T-MoS_2,[29] which was also manifested by UV-Vis electronic absorption spectroscopy – *vide supra*. Concerning MoS_2/rGO, Raman spectra revealed characteristic modes due to both components, regardless of the ratio employed between the inorganic precursor ATTM and GO for the preparation of the hybrid. Specifically, in the Raman spectrum of **1** (Fig. 2), the aforementioned characteristic bands owed to MoS_2 were observed. Similar vibrational modes were also observed for untemplated MoS_2. Furthermore, focusing in the frequency range of C–C vibrations, the characteristic D and G bands of rGO were present at 1329 and 1598 cm^{-1}, respectively. The intensity ratio of those two bands, $I_{D/G}$, was found to be 1.6, enhanced by 25% as compared to the one registered for intact GO (*i.e.* 1.28). The latter was expected, since microwave irradiation employed for the preparation of the hybrid material resulted to simultaneous removal of the oxygen-related species on GO, with subsequent establishment of small conductive graphene islands.[30] The Raman spectra of the different MoS_2/rGO hybrid materials **2–6** presented similar features with those of **1** (Fig. S6, ESI†).

The morphology of the MoS_2/rGO nanostructures was assessed by electron microscopy imaging. Specifically, Fig. 3a

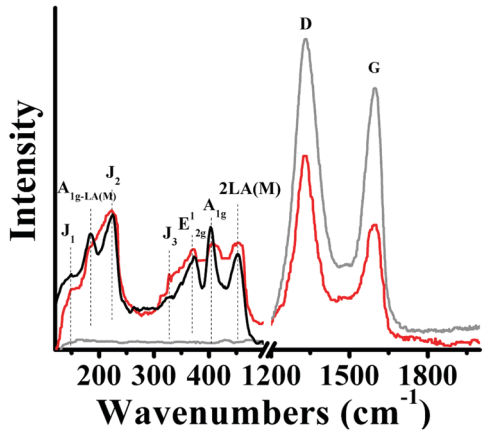

Fig. 2 Raman spectra (633 nm) for MoS_2/rGO hybrid material **1** (red), untemplated MoS_2 (black) and GO (grey).

shows a typical SEM image of material **1**. From the extensive imaging performed, it was clear that the majority of nanostructures were entangled graphene sheets with a minor content of inorganic component – see an isolated island of a MoS_2-based assembly in Fig. 3a. The stacking motif of MoS_2 sheets supported onto graphitic lattice was assessed by TEM imaging. Curled assemblies of intertwined inorganic flakes were observed for material **1** (Fig. 3b), which is a strong indication for the presence of defect-rich MoS_2 component. Similar assemblies were observed for **5** (Fig. 3c). Conversely, when the sacrificial template $CaCO_3$ was employed in the microwave-assisted reduction of ATTM salt to MoS_2, the latter was isolated after extensively washing the adduct with acidic water. The morphology of the resulting nanostructures sa-MoS_2 is presented in Fig. 3d. The majority of the objects identified were small-sized aggregated nanoparticles. The small size may be explained considering that MoS_2 growth occurs in a somewhat confined environment, in the vicinity of excess $CaCO_3$ crystallites within the liquid medium. Beyond those small-sized nanostructures for sa-MoS_2, one-dimensional nanorods were also observed (Fig. 3e and f). The length of these morphologies ranged to be 200 nm to 10 μm, while their diameter was approximately 20–100 nm. Additional TEM images of such sa-MoS_2 rod-like nanostructures are illustrated at the ESI† (Fig. S7).

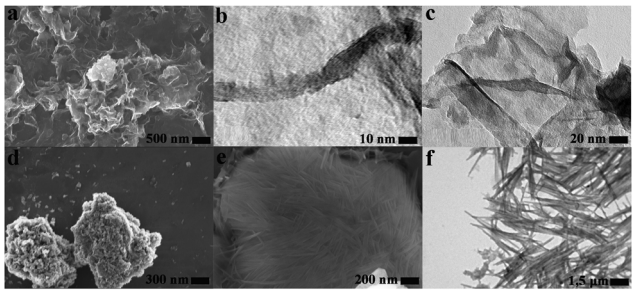

Fig. 3 (a) SEM image of MoS_2/rGO **1**. (b and c) TEM images of **1** and **5**, respectively. (d and e) SEM images of sa-MoS_2 showing small-sized aggregated nanoparticles, and nanorod morphology, respectively. (f) TEM image of sa-MoS_2 with nanorod morphology.

The electrocatalytic activity towards HER for all hybrid materials was investigated by linear sweep voltammetry (LSV). The assays were performed with a rotating-disc working glassy carbon electrode in a standard three-electrode glass cell at a scan rate of 5 mV s^{-1} in N_2 saturated 0.5 M H_2SO_4. Fig. 4a and Fig. S8a (ESI†) illustrate polarization curves for the different MoS_2/rGO hybrids, in comparison with those of untemplated MoS_2, sa-MoS_2, GO and commercial Pt (20% on carbon). Apparently, the electrocatalytic activity of MoS_2/rGO hybrids **1–6** was significantly increased compared to that of untemplated MoS_2, sa-MoS_2 and GO, as evidenced by the increase of the cathodic current at a given potential. Markedly, the highest onset overpotential among the different MoS_2/rGO hybrids was registered for **1** at −0.09 V *vs.* RHE (Fig. 4b), shifted by 300 mV to more positive potentials as compared to that of untemplated MoS_2, appearing at −0.390 V *vs.* RHE and Pt exhibiting the highest HER catalytic performance at 0.026 V overpotential. Fig. 4b and Fig. S8b (ESI†) summarize the onset overpotentials for all tested materials, showcasing the beneficial role of rGO for enhancing the electrocatalytic activity of MoS_2 towards HER under optimized conditions. Noting that the amount of cathodic current density is proportional to the amount of hydrogen evolved and since HER electrocatalysts are commonly compared against overpotential at a cathodic current density of 10 mA cm^{-2}, Fig. 4c and Fig. S8c (ESI†) collectively illustrate a graph of those parameters for all materials. Again, **1** exhibited among all tested hybrids the best electrocatalytic activity at 0.154 V, by showing a more positive potential by 476 mV as compared to that of untemplated MoS_2 at the cathodic current density of 10 mA cm^{-2}. Overall, the enhanced electrocatalytic activity for MoS_2 hybridized with rGO is attributed to a combination of factors, namely the metallic nature of MoS_2 and intimate contact with rGO, the absence of any organic species and/or surfactants, and the enhanced number of exposed edge sites in MoS_2.

In order to decode the HER mechanism and determine the rate limiting step, the Tafel slope for all tested materials was extracted from the LSV polarization curves and presented in Fig. 4d and Fig. S8d (ESI†). Briefly, all MoS_2/rGO hybrids exhibited smaller Tafel slope as compared to that owed to untemplated MoS_2 and sa-MoS_2, indicating that for the generation of an equivalent current only a lower overpotential is required.

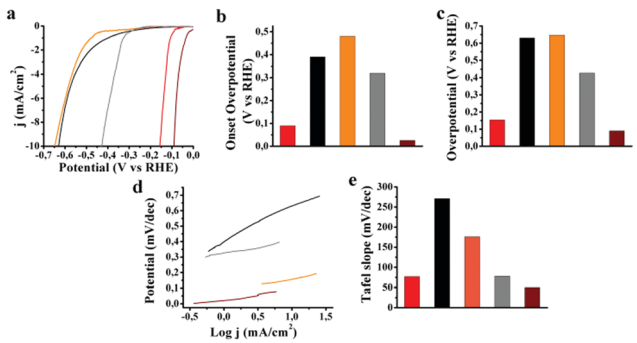

Fig. 4 (a) LSV for HER polarization curves. (b and c) Graphs for onset overpotential, and overpotential registered at −10 mA cm^{-2} current density, respectively. (d and e) Tafel slopes, and tabulated values. Color code: MoS_2/rGO material **1** (red), untemplated MoS_2 (black), sa-MoS_2 (orange), GO (grey), and Pt/C (wine).

Hence, the electrocatalytic activity of MoS_2/rGO was enhanced in comparison to untemplated MoS_2 and sa-MoS_2, which can be rationalized by considering good electrical contact between the two species within the MoS_2/rGO hybrid. Generally, three possible reaction steps are considered for the HER in acidic media.[31] First, the adsorption of a proton onto the electrode surface *via* a reduction process (Volmer adsorption) takes place. Next, bonding of the adsorbed hydrogen with a proton and electron transfer from the electrode surface (Heyrovsky desorption), or recombination of two hydrogen atoms adsorbed on the electrode surface (Tafel desorption), occurs. Based on the tabulated Tafel slope values given in Fig. 4e, the electrochemical desorption of adsorbed hydrogen atoms from the modified electrode surface governs the rate limiting step for MoS_2/rGO hybrid material **1**. On the contrary, the Tafel slope for untemplated MoS_2 and sa-MoS_2, is higher, attributing the rate-limiting step to the adsorption of hydrogen onto the electrode surface. Similar is the situation for MoS_2/rGO materials **2–6** (Fig. S8e, ESI†).

In order to shed light on the enhanced electrocatalytic activity of the MoS_2/rGO hybrid materials, the electrochemically active surface area (ECSA) was calculated (see ESI† for details) by performing cyclic voltammetry in a non-faradaic region at different scan rates (Fig. S9, ESI†). Apparently, the ECSA values of MoS_2/rGO were significantly higher than that of untemplated MoS_2 and sa-MoS_2 (Table S1, ESI†). In line with the rest electrochemical results, **1** exhibits the higher ECSA value – note that hybrids with higher ECSA values indicate more effective accessibility of the active sites, similarly with recent reports.[32] Lastly, durability studies were performed to evaluate their long-term stability. To assess this, continuous cyclic voltammograms were implemented (Fig. S10, ESI†), where negligible loss of the cathodic current was observed for all tested materials. The various HER parameters before and after 1000 cycles are summarized in Table S1 (ESI†).

In summary, the microwave-assisted synthesis of defect-rich MoS_2 nanostructures by adopting a sacrificial template approach based on $CaCO_3$ and a hard template one based on GO was studied. The starting composition of precursor components was varied in a wide range of mass ratios. Among the tested nanostructures as HER electrocatalysts, the optimized MoS_2/rGO material **1** showed improved electrocatalytic performance, requiring an overpotential of 154 mV at a current density of 10 mA cm^{-2} and showing a Tafel slope of 77 mV dec^{-1}. The enhanced electrocatalytic functioning of MoS_2/rGO was ascribed to the (a) metallic nature of MoS_2 and intimate contact with rGO, (b) the absence of any organic species and/or surfactants, and (c) the enhanced number of exposed edge sites in MoS_2. The higher ECSA value for **1** points out the large functioning surface area of the catalytic active sites and the excellent hydrogen production ability that leads to superior catalytic performance. Furthermore, examination of the Tafel slopes, manifested the adsorption of hydrogen as the rate-limiting step for hydrogen generation.

Funding from EC H2020 Marie Sklodowska-Curie grant agreement 642742, projects ''Advanced Materials and Devices'' (MIS 5002409) and ''National Infrastructure in Nanotechnology, Advanced Materials and Micro-/Nanoelectronics'' (MIS 5002772) co-financed by Greece and EU (European Regional Development Fund) is acknowledged. We thank Prof. A. Avgeropoulos (Department of Materials Science & Engineering, University of Ioannina) for TEM images acquisition.

Conflicts of interest

There are no conflicts to declare.

Notes and references

1 G. Pagona, C. Bittencourt, R. Arenal and N. Tagmatarchis, *Chem. Commun.*, 2015, **51**, 12950–12953.
2 J. Zheng, H. Zhang, S. Dong, Y. Liu, C. T. Nai, H. S. Shin, H. Y. Jeong, B. Liu and K. P. Loh, *Nat. Commun.*, 2014, **5**, 2995.
3 Y. Yao, L. Torentino, Z. Yang, X. Song, W. Zhang, Y. Chen and C. Wong, *Adv. Funct. Mater.*, 2013, **23**, 3577–3583.
4 G. Eda, H. Yamaguchi, D. Voiry, T. Fujita, M. Chen and M. Chhowalla, *Nano Lett.*, 2011, **11**, 5111–5116.
5 Y. Ling, Z. Yang, Q. Zhang, Y. Zhang, W. Cai and H. Cheng, *Chem. Commun.*, 2018, **54**, 2631–2634.
6 E. E. Benson, H. Zhang, S. A. Schuman, S. U. Nanayakkara, N. D. Bronstein, S. Ferrere, J. L. Blackburn and E. M. Miller, *J. Am. Chem. Soc.*, 2018, **140**, 441–450.
7 R. Canton-Vitoria, L. Vallan, E. Urriolabeitia, A. M. Benito, W. K. Maser and N. Tagmatarchis, *Chem. – Eur. J.*, 2018, **24**, 10468–10474.
8 M.-R. Gao, M. K. Y. Chan and Y. Sun, *Nat. Commun.*, 2015, **6**, 7493.
9 X. Chia, A. Y. S. Eng, A. Ambrosi, S. M. Tan and M. Pumera, *Chem. Rev.*, 2015, **115**, 11941–11966.
10 D. Voiry, J. Yang and M. Chhowalla, *Adv. Mater.*, 2016, **28**, 6197–6206.
11 J. Yang and H. S. Shin, *J. Mater. Chem. A*, 2014, **2**, 5979–5985.
12 L. Cheng, W. Huang, Q. Gong, C. Liu, Z. Liu, Y. Li and H. Dai, *Angew. Chem., Int. Ed.*, 2014, **53**, 7860–7863.
13 D. Voiry, M. Salehi, R. Silva, T. Fujita, M. Chen, T. Asefa, V. B. Shenoy, G. Eda and M. Chhowalla, *Nano Lett.*, 2013, **13**, 6222–6227.
14 M. A. Lukowski, A. S. Daniel, F. Meng, A. Forticaux, L. Li and S. Jin, *J. Am. Chem. Soc.*, 2013, **135**, 10274–10277.
15 J. Kibsgaard, Z. Chen, B. N. Reinecke and T. F. Jaramillo, *Nat. Mater.*, 2012, **11**, 963–969.
16 Y. Li, H. Wang, L. Xie, Y. Liang, G. Hong and H. Dai, *J. Am. Chem. Soc.*, 2011, **133**, 7296–7299.
17 A. Ciarrocchi, A. Avsar, D. Ovchinnikov and A. Kis, *Nat. Commun.*, 2018, **9**, 919.
18 T. F. Jaramillo, K. P. Jorgensen, J. Bonde, J. H. Nielsen, S. Horch and I. Chorkendorff, *Science*, 2007, **317**, 100–102.
19 G. Ye, Y. Gong, J. Lin, B. Li, Y. He, S. T. Pantelides, W. Zhou, R. Vajtai and P. M. Ajayan, *Nano Lett.*, 2016, **16**, 1097–1103.
20 J. Xie, H. Zhang, S. Li, R. Wang, X. Sun, M. Zhou, J. Zhou, X. W. Lou and Y. Xie, *Adv. Mater.*, 2013, **25**, 5807–5813.
21 K. D. Rasamani, F. Alimohammadi and Y. Sun, *Mater. Today*, 2017, **20**, 83–91.
22 M. Chatti, T. Gengenbach, R. King, L. Spiccia and A. N. Simonov, *Chem. Mater.*, 2017, **29**, 3092–3099.
23 Q. Wei, M.-R. Gao, Y. Li, D. Zhang, S. Wu, Z. Chen and Y. Sun, *Mater. Chem. Front.*, 2018, **2**, 1441–1448.
24 Y. Sun, F. Alimohammadi, D. Zhang and G. Guo, *Nano Lett.*, 2017, **17**, 1963–1969.
25 Y. Ji, Q. Wei and Y. Sun, *Ind. Eng. Chem. Res.*, 2018, **57**, 4571–4576.
26 K. S. Andrikopoulos, G. Bounos, D. Tasis, L. Sygellou, V. Drakopoulos and G. A. Voyiatzis, *Adv. Mater. Interfaces*, 2014, **1**, 1400250.
27 C.-H. Lin, C.-H. Tsai, F.-G. Tseng, Y.-Y. Yu, H.-C. Wu and C.-K. Hsieh, *Nanoscale Res. Lett.*, 2015, **10**, 446.
28 L. Sygellou, G. Paterakis, C. Galiotis and D. Tasis, *J. Phys. Chem. C*, 2016, **120**, 281–290.
29 A. P. Nayak, T. Pandey, D. Voiry, J. Liu, S. T. Moran, A. Sharma, C. Tan, C.-H. Chen, L.-J. Li, M. Chhowalla, J.-F. Lin, A. K. Singh and D. Akinwande, *Nano Lett.*, 2015, **15**, 346–353.
30 Y. Zhang, H.-L. Ma, Q. Zhang, J. Peng, J. Li, M. Zhai and Z.-Z. Yu, *J. Mater. Chem.*, 2012, **22**, 13064–13069.
31 B. E. Conway and B. V. Tilak, *Electrochim. Acta*, 2002, **47**, 3571–3594.
32 B. You, N. Jiang, M. Sheng, W. Bhushan and Y. Sun, *ACS Catal.*, 2016, **6**, 714–722.